PAPER • OPEN ACCESS

Magnetization dynamics in an exchange-coupled NiFe/CoFe bilayer studied by x-ray detected ferromagnetic resonance

To cite this article: G B G Stenning *et al* 2015 *New J. Phys.* **17** 013019

New Journal of Physics
The open access journal at the forefront of physics

Deutsche Physikalische Gesellschaft DPG
IOP Institute of Physics

Published in partnership with: Deutsche Physikalische Gesellschaft and the Institute of Physics

OPEN ACCESS

RECEIVED
2 October 2014

ACCEPTED FOR PUBLICATION
8 December 2014

PUBLISHED
15 January 2015

PAPER

Magnetization dynamics in an exchange-coupled NiFe/CoFe bilayer studied by x-ray detected ferromagnetic resonance

G B G Stenning[1,2], L R Shelford[3], S A Cavill[4], F Hoffmann[5], M Haertinger[5], T Hesjedal[6], G Woltersdorf[7], G J Bowden[1], S A Gregory[1], C H Back[5], P A J de Groot[1] and G van der Laan[3]

[1] School of Physics and Astronomy, University of Southampton, SO17 1BJ, UK
[2] ISIS, Rutherford Appleton Laboratory, Didcot, OX11 0QX, UK
[3] Magnetic Spectroscopy Group, Diamond Light Source, Didcot, OX11 0DE, UK
[4] Department of Physics, University of York, York, YO10 5DD, UK
[5] Universität Regensburg, Universitätsstrasse 31, D-93040 Regensburg, Germany
[6] Clarendon Laboratory, Department of Physics, University of Oxford, Oxford, OX1 3PU, UK
[7] Martin-Luther-Universität Halle-Wittenberg, Institute of Physics, Halle, Germany

E-mail: Gerrit.vanderLaan@diamond.ac.uk

Keywords: FMR, magnetism, XMCD, exchange coupling

Abstract

Exchange-coupled hard and soft magnetic layers find extensive use in data storage applications, for which their dynamical response has great importance. With bulk techniques, such as ferromagnetic resonance (FMR), it is difficult to access the behaviour and precise influence of each individual layer. By contrast, the synchrotron radiation-based technique of x-ray detected ferromagnetic resonance (XFMR) allows element-specific and phase-resolved FMR measurements in the frequency range 0.5–11 GHz. Here, we report the study of the magnetization dynamics of an exchange-coupled $Ni_{0.81}Fe_{0.19}$ (43.5 nm)/$Co_{0.5}Fe_{0.5}$ (30 nm) bilayer system using magnetometry and vector network analyser FMR, combined with XFMR at the Ni and Co L_2 x-ray absorption edges. The epitaxially grown bilayer exhibits two principal resonances denoted as the acoustic and optical modes. FMR experiments show that the Kittel curves of the two layers cannot be taken in isolation, but that their modelling needs to account for an interlayer exchange coupling. The angular dependence of FMR indicates a collective effect for the modes of the magnetically hard CoFe and soft NiFe layer. The XFMR precessional scans show that the acoustic mode is dominated by the Ni signal with the Co and Ni magnetization precessing in phase, whereas the optical mode is dominated by the Co signal with the Co and Ni magnetization precessing in anti-phase. The response of the Co signal at the Ni resonance, and vice versa, show induced changes in both amplitude and phase, which can be ascribed to the interface exchange coupling. An interesting aspect of phase-resolved XFMR is the ability to distinguish between static and dynamic exchange coupling. The element-specific precessional scans of the NiFe/CoFe bilayer clearly have the signature of static exchange coupling, in which the effective field in one layer is aligned along the magnetization direction of the other layer.

1. Introduction

In recent years, multilayers consisting of alternating hard and soft magnetic layers have attracted a great deal of attention due to their potential applications in data storage media [1–3], permanent magnets [4, 5], and microelectromechanical systems [6–8]. In particular, bilayer systems composed of exchange-coupled hard and soft layers have been proposed as superior data storage media because they can be used to overcome the so-called super-paramagnetic limit, while retaining relatively low writing fields [9]. Further, exchange coupling between layers can lead to increased damping [10] and faster writing speeds due to higher resonance frequencies. For such applications it is important to gain detailed knowledge of the magnetization dynamics in the different

layers. Here, we focus on the study of a bilayer system consisting of a magnetically soft NiFe layer, exchange-coupled to a harder CoFe layer.

In the past, ferromagnetic resonance (FMR) has been widely used to study magnetization dynamics of multilayer systems [11–15] and exchange-coupled bi- and trilayer systems [16–18]. Both broadband coplanar waveguide (CPW) and resonant cavity FMR techniques are commonly employed. However, these methods are limited in that they can only detect the net response of the multilayer sample. In practice, the response of individual layers can only be inferred indirectly by comparing the experimental FMR spectra with micromagnetic modelling [14]. Recently, x-ray detected FMR (XFMR) has emerged as a powerful synchrotron radiation based tool that can be used to study the element-selective magnetization dynamics [19–32]. Magnetic and chemical contrast in XFMR is obtained by x-ray magnetic circular dichroism (XMCD) [33, 34], while phase differences in the magnetization precessions can be monitored using a stroboscopic measurement technique. The element specificity of XFMR offers clear advantages over FMR, in particular, it allows layer resolution of the magneto-dynamics in multilayer samples.

Spin valve type structures, in which two ferromagnetic layers are separated by a thin layer of normal metal such as Cu, have been studied by XFMR [30, 31, 35, 36]. Bailey *et al* [31] reported an unexpectedly large phase variation of ~40° across a spin valve trilayer driven at 3 GHz. Marcham *et al* [30] used phase-resolved XFMR to confirm the spin pumping effect in a spin value structure. By recording the phase of precession of the CoFe fixed layer as the NiFe free layer is swept through the FMR condition a clear signature of spin transfer torque (STT) was observed. Fitting the amplitude and phase delay yielded the value of the spin mixing conductance [30], which is the quantity that controls all spin transfer phenomena [37]. So far, XFMR has not been reported for strongly exchange coupled bilayers, partly because the higher resonance frequencies required for such measurements are not attainable at some synchrotron facilities [38].

In this paper we present an XFMR study on a NiFe (43.5 nm)/CoFe (30 nm) bilayer, detected at the photon energies of the Ni and Co L_2 x-ray absorption edges. The observation of the CoFe layer resonance requires a radio-frequency (RF) of 8 GHz or above. To characterize the bilayer we performed an extensive magnetization study including hysteresis loop magnetometry, vector network analyser (VNA)–FMR of the frequency versus applied field (ν-B_a) transmission and the angular dependence. The results reveal the influence of the CPW patterning, magnetic anisotropy, and interlayer exchange coupling. The XFMR enables element-specific field and time-delay scans. The obtained precessional scans show that the two ferromagnetic layers are strongly coupled by static interlayer exchange interaction.

2. Methods

2.1. Sample preparation

Epitaxial $Co_{0.5}Fe_{0.5}$ and $Ni_{0.81}Fe_{0.19}$ layers were grown on MgO (001) substrates measuring 10×12 mm^2 in a molecular beam epitaxy (MBE) system (base pressure 5×10^{-10} Torr). After degreasing, the MgO substrates are annealed at 700 °C until the expected diffraction pattern is observed by reflection high-energy electron diffraction (RHEED). After cool-down to room temperature, 3 nm of Fe seed layer and 30 nm of Pt buffer layer were deposited at a rate of 0.1 Å s^{-1}, followed by an anneal at 500 °C leading to a streaky RHEED pattern. The Fe and Pt layers are inserted for strain accommodation reasons, reducing the MgO lattice constant of 4.213 Å more gradually towards the 3.55 Å of $Ni_{0.81}Fe_{0.19}$. After cool-down to 100 °C, 43.5 nm of $Ni_{0.81}Fe_{0.19}$ and 30 nm of $Co_{0.5}Fe_{0.5}$ were grown at a rate of 0.5 Å s^{-1} and 0.6 Å s^{-1}, respectively. Owing to the low-temperature growth, the RHEED patterns gradually change from streaks to streaky spots. To prevent the sample from oxidation, a 5 nm thin, amorphous Pt cap was deposited at room temperature. The epitaxial relationship of the NiFe/CoFe bilayer stack is MgO(001)[100]‖ Fe(001)[110] (3 nm)‖ Pt(001)[100] (30 nm)‖ $Ni_{0.81}Fe_{0.19}$(001)[100] (43.5 nm)‖ $Co_{0.5}Fe_{0.5}$(001)[110] (30 nm) /Pt (5 nm). The in-plane rotation is due to the transition from bcc Fe, to fcc Pt and fcc $Ni_{0.81}Fe_{0.19}$, back to bcc $Co_{0.5}Fe_{0.5}$. The MBE grown films have atomically abrupt interfaces and well-defined anisotropies. The given thicknesses of the NiFe and CoFe layers were determined by polarized neutron reflectivity (not shown).

The bilayer was oriented with respect to the CPW with the transmission line along the $Co_{0.5}Fe_{0.5}$(001)[110] direction, which corresponds to the easy axis [39]. In the angular dependent measurements the field was applied at an angle β with respect to the MgO[100] direction in the (001) plane (cf figure 1).

2.2. VNA–FMR technique

Prior to the XFMR experiments, the sample was characterized using VNA–FMR [40]. To achieve good coupling with the RF waves the bilayer sample was placed top–down directly onto the CPW ('flip-chip' method) [41] and then positioned in the electromagnet. A VNA (Agilent HP E5071C) was used to determine the scattering parameter S_{21} of the system, which is proportional to the amount of RF absorption in the sample. In particular,

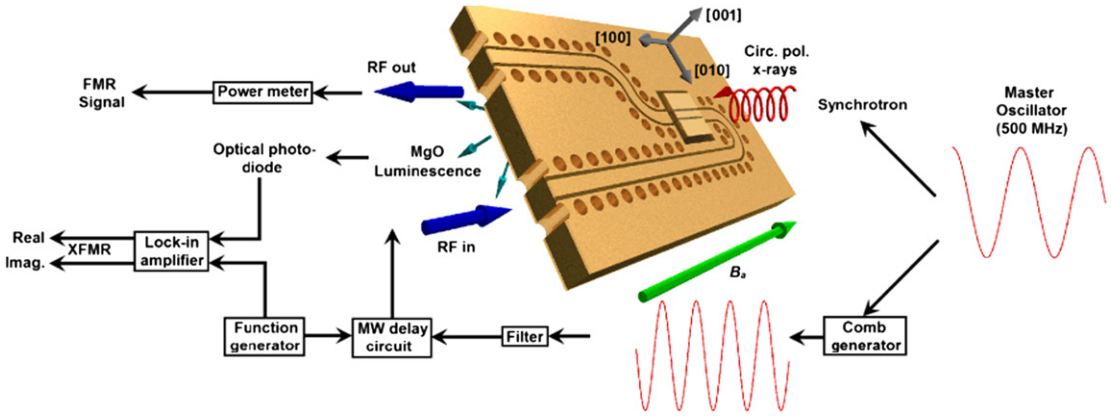

Figure 1. Schematic representation of the sample mounted onto a CPW (within the POMS chamber, which provides the magnetic field). The holes (vias) improve the RF transmission by electrically connecting conducting planes on the upper and lower surfaces of the CPW. The depicted coordinate frame refers to the crystalline axes for the MgO(001) substrate of the sample with epitaxial relationship MgO(001)[100] || NiFe(001)[100] || CoFe(001)[110]. The plane of the bilayer sample was set to 30°. The applied field B_a is perpendicular to the x-ray beam direction and along the CPW transmission line (in the default geometry with $\beta = 0°$). The XFMR electronic signal circuitry, RF excitation circuit, and x-ray detection system are also shown. A delay line enables phase shifting of the RF oscillation with respect to the x-ray pulses with 0.5 ps step resolution.

two-dimensional ν-B_a maps of S_{21} were obtained as a function of driving frequency ν and applied field B_a. This allowed us to identify the resonance modes and to map-out the magnetic anisotropy by rotating the applied field with respect to the crystal axes of the bilayer sample.

2.3. CPW patterning for XFMR

For the XFMR measurements a straight CPW structure was patterned on the bilayer in order to carry the RF current while allowing x-ray transmission. 100 nm Cu was deposited onto the sample by e-beam evaporation with a 500 μm wide signal line patterned through all the layers to the substrate with gaps of 200 μm either side until the ground plane is reached. Patterning was performed by photolithography and Ar ion beam etching, with CPW dimensions set by calculation to give a characteristic impedance $Z_0 = 50\ \Omega$. Passing RF current through the Cu overlayer favours in-phase excitation of the NiFe and CoFe layers [19], while the Cu remains thin enough to allow the transmission of soft x-rays. The RF field produced by the CPW is given by $B_{\mathrm{RF}}^{\mathrm{rms}} = \mu_0/(2W)\sqrt{P/Z_0}$ [28], where W (=500 μm) is the CPW centre conductor width, giving an rms RF field of 175 μT for a driving power $P = 1$ W. The patterned sample was mounted to a CPW formed from a printed circuit board, and electrically contacted using wire bonding.

2.4. XFMR technique

2.4.1. XFMR principle

The dynamical process of spin precession is detected using element-specific XMCD [42]. We recall that static XMCD is obtained as the difference between the two x-ray absorption spectra with the helicity vector of the circular polarization parallel and antiparallel respectively to an external magnetic field [34]. The XMCD signal is proportional to the projection of the helicity vector, which is along the beam direction $\hat{\mathbf{k}}$, onto the magnetization $\mathbf{M}$, hence $I_{\mathrm{XMCD}} \propto \hat{\mathbf{k}} \cdot \mathbf{M}$. The same XMCD spectrum can be obtained by reversing either the magnetic field or the circular polarization direction in the experimental geometry. In the XFMR technique, we use the XMCD effect to measure with fixed circular polarization the small periodic oscillations in the magnetization direction.

The magnetization dynamics can be described by the Landau–Lifshitz (LL) equation [43]. Applying a bias field B_a to obtain a magnetization M along the z-axis, a small transverse RF field $B_y^{\mathrm{RF}}(t) = B^{\mathrm{RF}} \exp(\mathrm{i}\omega t)$ along the y-axis will drive the magnetization in precession about the z-axis at the angular frequency ω_0 of the resonance. According to the Kittel equation [44], $\omega_0 = \gamma\mu_0\sqrt{H_{\mathrm{eff}}(H_{\mathrm{eff}} + M_0)}$, where γ is gyromagnetic ratio, μ_0 is the vacuum permeability, H_{eff} is the effective magnetization, and M_0 is the saturation magnetization. Linearization of the LL equation gives a damped harmonic oscillator with amplitude A and phase ϕ given as $|A| \approx \gamma\mu_0\sqrt{M_0 H_y/[(\omega - \omega_0)^2 + \lambda^2\omega^2]}$ and $\tan\phi = \lambda\omega/(\omega - \omega_0)$, where λ is the relaxation rate in s^{-1}. The precessing magnetization traces out a cone with angle θ, reducing the z-axis projection to $M_z = M_0\cos\theta$. Orthogonal to the bias field, the magnetization varies periodically in time with $M_y(t) = M_0 \sin\theta\cos(\omega t - \phi)$.

There are two principal methods to measure XFMR, namely time-averaged using a longitudinal geometry ($\hat{\mathbf{k}} \parallel \mathbf{B}_a$) [20, 24] and time-resolved using a transverse geometry ($\hat{\mathbf{k}} \perp \mathbf{B}_a$) [28]. In time-averaged XFMR, the

shortening of the magnetization vector along the z-axis leads to a difference $\Delta M_z = M_0(1 - \cos\theta) \approx \frac{1}{2}M_0\theta^2$. The time-averaged XFMR requires no synchronization with the synchrotron, which means it can be measured at any frequency, provided the RF power is sufficiently strong.

In this study, the XFMR is measured in the time-resolved mode, which gives access to the precessional phase. With the bias field perpendicular to the incident x-ray beam, the oscillating component of the Larmor precession is observed with a magnitude $|M_y| = M_0 \sin\theta \approx M_0\theta$. Thus the XFMR signal in transverse geometry also has the advantage that it is larger than in longitudinal geometry by a factor $2\theta^{-1}$. At the resonance frequency the cone angle θ is typically in the order of 10 mrad (≈0.57°) [23, 45], resulting in a dynamic XMCD in transverse and longitudinal geometry of 1% and 0.005%, respectively, of the static XMCD. The precession angle is strongly elliptical due to the shape anisotropy of the film. We can expect a larger amplitude in the plane (M_y) than normal to the plane (M_x), hence this favours a measurement geometry where the x-rays are incident at grazing angle. The time-resolved XFMR is detected stroboscopically by using the periodic x-ray pulses from the synchrotron. The RF is fixed to a multiple of the x-ray pulse frequency (499.65 MHz) and the applied field can be used to tune the resonance.

2.4.2. XFMR setup

Time-resolved XFMR measurements were performed on beamline I06 at Diamond Light Source and on beamline PM3 (dipole PGM variable polarization) at BESSY II of the Helmholtz-Zentrum Berlin. A schematic of the experimental setup can be seen in figure 1 (see also references [26, 28, 29, 35] for alternative approaches). At Diamond, the bias field was supplied using the portable octupole magnet system, in which the field can be applied in any direction up to 0.9 T [46]. The vector magnet is particularly suitable for XFMR as it allows a simple change of B_a from (i) parallel to the photon direction, which is needed for static XMCD scans to (ii) orthogonal to both the photon direction and the RF excitation, required for phase-resolved XFMR. The vector electromagnet design consists of eight current coils, positioned externally along the three-fold axes of the six-way-cross vacuum chamber, which allows free access for the x-ray beam and the sample manipulator. At BESSY two sets of orthogonal Helmholtz coils, mounted inside the vacuum chamber, were used to apply a longitudinal or transverse bias field.

For the stroboscopic measurements, the RF has to be a harmonic of x-ray pulse frequency, hence the resonance is driven at multiples of the master oscillator clock of the storage ring. These higher harmonics are generated using an RF comb generator (Atlantic Microwave) driven by the master oscillator, which has a frequency of 499.65 MHz, both at Diamond and BESSY II, corresponding to ∼2 ns intervals between consecutive x-ray pulses. The desired frequency is selected using filters and amplifiers to drive a narrow band, high power (25–30 dBm) RF field to the CPW. A programmable delay line (Colby Instruments) enables phase shifting of the RF oscillation with respect to the x-ray pulses with a step resolution of ∼0.5 ps. The timing jitter of the master oscillator signal measured using a spectrum analyser was found to be small (<0.5 ps). A limiting factor, determining the maximum RF (14 GHz) detectable by time-resolved XFMR, is the longitudinal photon bunch length (∼35 ps full width at half maximum in multibunch operation [47]). Other factors, such as increasing RF losses and a decreasing cone angle, bring the upper frequency of operation down to ∼11 GHz. The error in the phase oscillation (relative to the photon bunch clock) is determined by the total timing jitter over all components (< 1 ps, which is much smaller than photon bunch length of ∼35 ps). For instance, a 2 ps jitter at 8 GHz results in a lower limit of the phase resolution of ∼3°, provided a similar step size is used between the data points in the time-delay scan.

Incident x-rays impinge only on the central part of the CPW signal line patterned on the film, therefore avoiding non-uniform RF excitation [14]. The magnetization precession is detected by measuring its rotating component normal to the static magnetic field, in the transverse geometry, where the x-ray beam is perpendicular to the bias field (as explained in section 2.4.1, see also figure 1). The x-ray beam has an incidence angle of 30° with respect to the plane of the sample, to ensure that the XMCD is sensitive to the larger in-plane component of the magnetization precession. The x-ray absorption was measured in transmission geometry by detecting the x-ray excited optical luminescence emerging from the MgO substrate [48], using a photodiode mounted behind the sample.

Small amplitude precession was measured using lock-in detection while modulating the phase of the driving RF field through 180°. For each point in an XFMR scan the signal at a photon energy below the x-ray absorption edge (background signal) is subtracted from that at the resonance to yield a relative XMCD signal. It was confirmed that the background signal was free from any RF cross-talk.

As will be illustrated in section 4, various kinds of measurement protocols can be performed at fixed frequency in transverse geometry by recording the XMCD signal at the photon energy of the selected x-ray absorption edge. *Field scans* are performed by sweeping the magnetic bias field at a constant delay time. The signal of the field scan will contain a mixture of the real and imaginary part of the element-specific magnetic

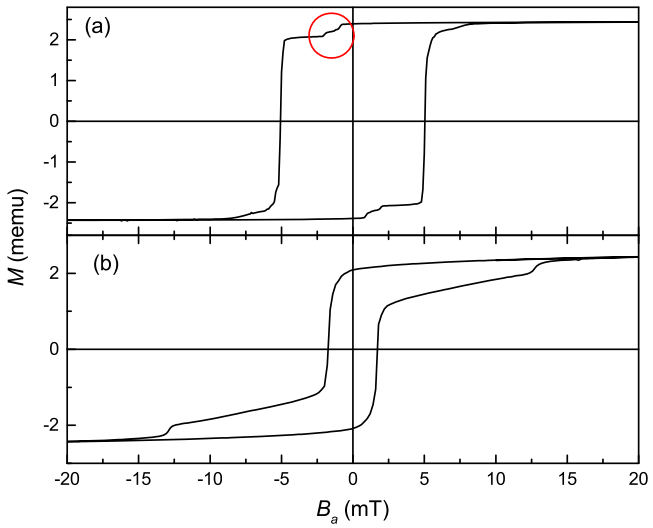

Figure 2. Magnetic hysteresis loop of the NiFe/CoFe bilayer with in-plane applied magnetic field along (a) easy axis and (b) hard axis of magnetization. The red marking circle shows the exchange spring behaviour at small field, as described in the text.

susceptibility, depending on the delay setting [28]. It is practical to set the delay time such that the peak at resonance is maximized. *Time-delay scans* are performed at constant bias field by sweeping the delay time. These delay scans map the element-specific magnetization precession, from which the amplitude and relative phase is extracted using a sinusoidal fit. Collecting the delay scans as a function of bias field gives the field dependence of amplitude and phase for each element, and we call this the *XFMR precessional scans*. By normalizing the XFMR signal to the static XMCD, the amplitude of the signal can be obtained per atom for each different chemical element in the sample. This allows a quantitative decomposition of the resonance features.

3. Characterization results

3.1. Superconducting quantum interference device (SQUID) magnetometry

Magnetic hysteresis loops of the NiFe/CoFe bilayer are shown in figure 2, obtained using a SQUID magnetometer. The transitions between the magnetization states in the double switching loop seen in figure 2(a) would be sharper if the magnetic layers were acting independently. The roundedness of the transition suggests a rotation of the magnetization (the red marking circle in figure 2(a)) until a sufficiently high field is reached to completely switch the respective layer. The hysteresis loop with the field applied along the in-plane hard axis is seen in figure 2(b), showing the characteristic shape of a bilayer sample.

3.2. VNA–FMR

Figure 3(a) shows the magnitude of the FMR signal as a function of frequency and applied field, with B_a along the easy axis ($\beta = 0°$). The horizontal streaks which appear across the ν-B_a map are parasitic resonances arising from the CPW cavity modes. Figure 3(b) shows the datapoints extracted from the ν-B_a map, together with the modelled curves which will be described in section 3.5. The measured resonance curves in figure 3(b) show a slight deviation from the fit at near zero field. We ascribe this to the presence of an exchange spring in the NiFe layer, pinned at the interface by the anisotropic CoFe layer (cf, red marking circle on hysteresis loop in figure 2(a)).

Two principal resonances can be observed, namely a low- and a high-frequency mode. It is customary in the literature to refer to these resonances as the acoustic and optical mode, respectively. Such a nomenclature is only sensible if the two modes are well separated from each other, which is the case here. As we will demonstrate by XFMR in section 4.2.2, in the acoustic mode the magnetization of the two layers precess in phase, while in the optical mode they process in anti-phase. Along the easy axis, the optical mode is only visible at frequencies above 9 GHz (figure 3).

3.3. FMR field sweeps

A cross-section of the ν-B_a map can be obtained by taking an individual field sweep at a constant frequency. Figures 4(a) and (b) displays FMR field sweeps at 9.5 GHz for the unpatterned and patterned sample, respectively, which show that there are differences in relative amplitudes for the observed modes. In the

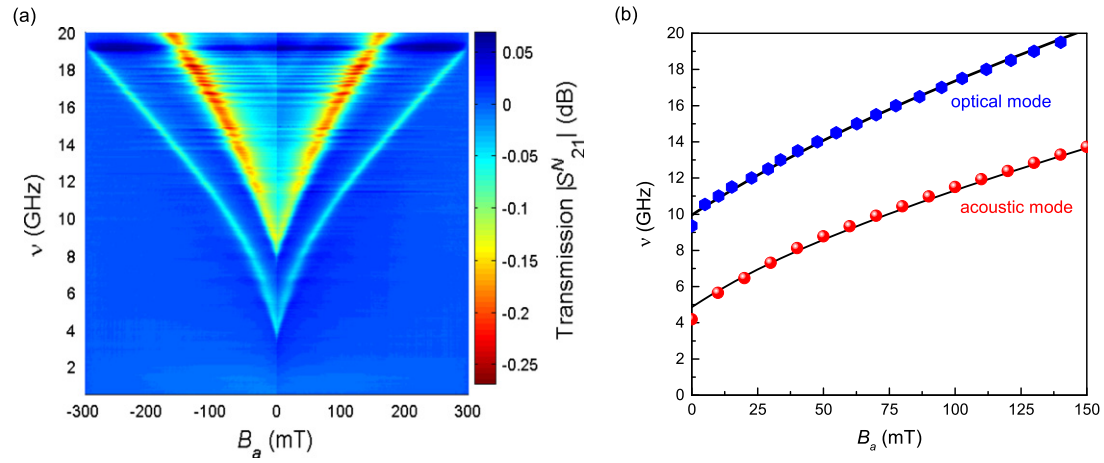

Figure 3. (a) Frequency versus field (ν-B_a) map measured by VNA–FMR with B_a along easy axis (ν is normalized at 0 T) showing the optical and acoustic modes of the NiFe/CoFe bilayer. (b) The resonance conditions extracted from (a) are shown by the symbols. The black lines give the result of modelling the two modes to the Kittel equation simultaneously with the magnetic anisotropy, which requires us to include the interlayer exchange coupling (see section 3.5 and table 1). The data points at lowest field value are below the coercive field, since the sweep was from negative to positive field.

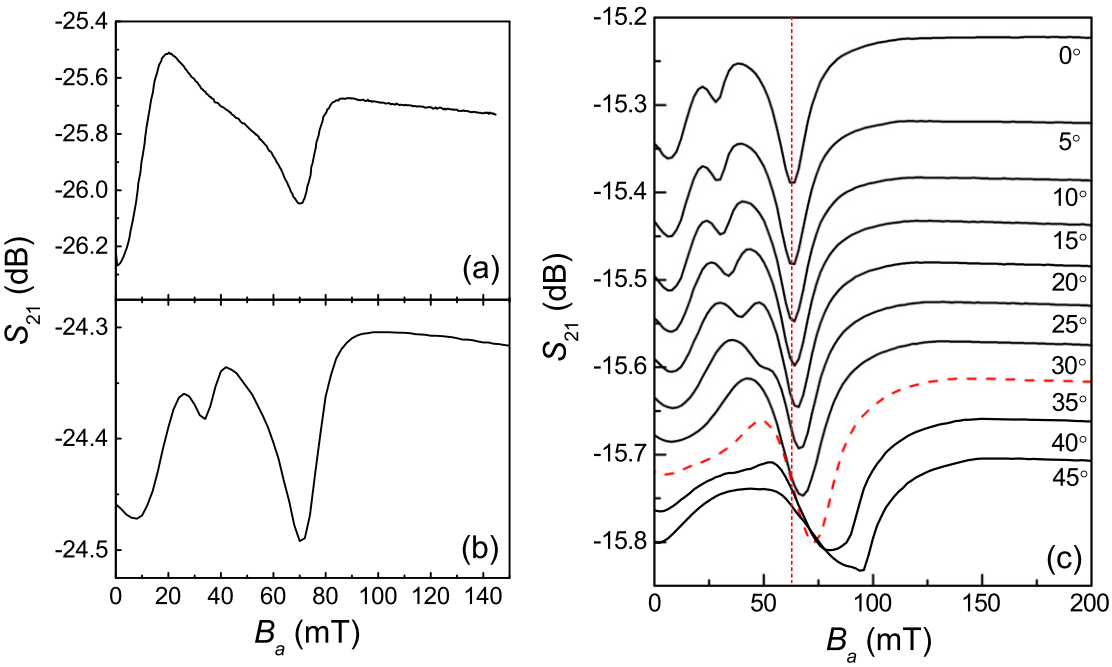

Figure 4. VNA–FMR field scans of the NiFe/CoFe bilayer at 9.5 GHz. Left panel: (a) unpatterned sample and (b) sample patterned into a CPW, where B_a is along the easy axis ($\beta = 0°$). (c) Patterned sample with in-plane magnetic field at an angle β with respect to the easy-axis (which is along the CPW transmission line). The dashed red curve for $\beta = 35°$ corresponds to the precessional scans shown in figure 9 (right panel). The transmission S_{21} (dB) is measured with respect to the unloaded experimental set-up at zero applied field.

patterned sample three modes are observed: apart from the optical mode at low field (~6.2 mT) and the acoustic mode at high field (~70 mT), there is also a middle mode (~33 mT). In section 4.2.1 we will demonstrate that these modes are mainly due to the CoFe, NiFe, and the Fe-seed layer, respectively. Applying an RF field to the patterned sample drives the buried NiFe and the Fe-seed layer with greater amplitude relative to the CoFe layer than in the 'flip-chip' geometry.

3.4. Angle-dependence of resonant frequency

The field sweeps in figure 4(c) for the patterned sample show the changes of the FMR signal under rotation of the magnetic field away from the easy axis. The in-plane magnetic field angle, β, is defined with respect to the easy magnetization direction of the CoFe layer, which is along the CPW transmission line.

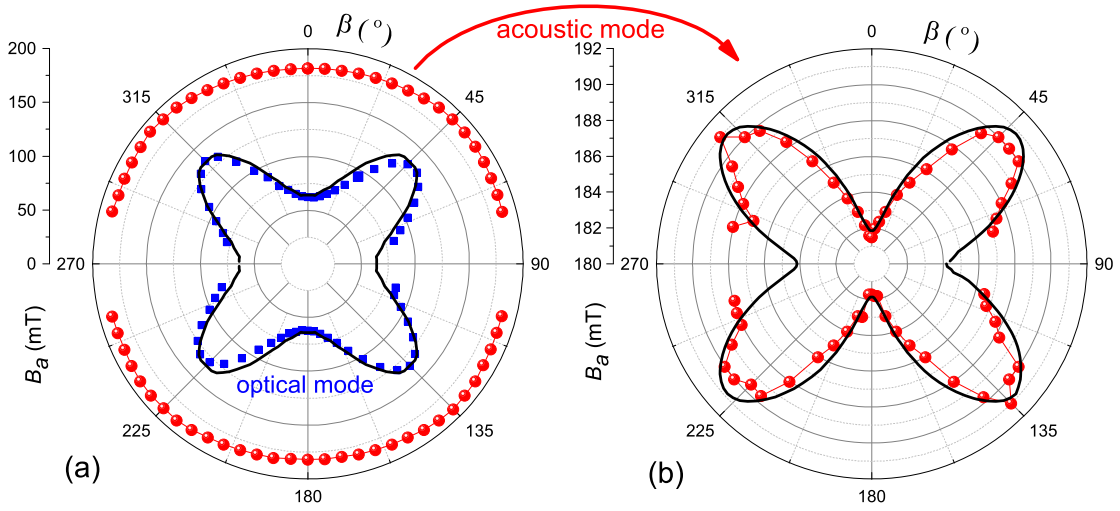

Figure 5. Magnetic anisotropy of the resonance modes measured by VNA–FMR at 15 GHz as a function of β, the angle of the applied field B_a with respect to the $Ni_{0.81}Fe_{0.19}$[100] || $Co_{0.5}Fe_{0.5}$[110] axes in the (001) plane. (a) Red (blue) corresponds to the acoustic (optical) mode, where the symbols represent experimental data points and thin lines are guides to the eye. (b) The acoustic mode shown on an expanded scale. For both modes the black lines give the result of the modelling including cubic and uniaxial anisotropies and interlayer exchange coupling (see table 1 for the extracted parameter values). The easy axes of both layers, where B_{res} has a minimum, are found at $\beta = 0°$.

The magnetic anisotropy of the bilayer was obtained by angle-dependent VNA–FMR measurements, sweeping the applied magnetic field at fixed frequency. To ensure that both resonant modes were clearly visible, the frequency was set to 15 GHz. Field sweeps were taken for β in steps of 5°. Subsequently, a Lorentzian line shape was fitted to the FMR peak and the resonance field was plotted as a function of the applied field angle, as shown in figure 5(a).

The optical mode (at low field) reveals a strong cubic anisotropy with easy axes along $\beta = 0°$ and 90° and hard axes along ±45°, relative to the $Co_{0.5}Fe_{0.5}$ [110] crystal axis. In contrast, the NiFe mode (at high field) gives a more isotropic behaviour. This suggest that the optical mode is predominantly driven by the CoFe, which is known to have a strong four-fold magnetic anisotropy. Figure 5(b) shows the acoustic mode on an expanded scale, which reveals a weak anisotropy deviating from a perfect circle for an isotropic medium. This mode is therefore predominantly driven by $Ni_{0.81}Fe_{0.19}$ (permalloy), which is known to possess a weak magnetic anisotropy. The NiFe shows both cubic and uniaxial anisotropy components with easy axes along $\beta = 0°$. The presence of uniaxial anisotropy suggests that the NiFe layer possesses an intrinsic two-fold anisotropy, perhaps induced during crystal growth [49, 50].

3.5. Modelling

The resonance angular frequency, $\omega_0 = 2\pi\nu$, for a uniform thin film layer with index i is given by the Kittel equation [44] (in SI units) as

$$\omega_0^i = \gamma\sqrt{H_{\text{eff}}^i B_{\text{eff}}^i} \tag{1}$$

with the effective magnetic field determined by the external, dipole, and anisotropy fields as

$$H_{\text{eff}}^i(\varphi) = \mu_0 H\cos(\varphi - \varphi_H) + \mu_0 H_{\text{ex}}^i\cos(\varphi - \varphi_{M^i}) + \frac{2K_{C\|}^i}{M_0^i}\cos 4(\varphi - \varphi_C) - \frac{2K_{U\|}^i}{M_0^i}\cos 2(\varphi - \varphi_U), \tag{2}$$

$$B_{\text{eff}}^i(\varphi) = \mu_0 H\cos(\varphi - \varphi_H) + \mu_0 H_{\text{ex}}^i\cos(\varphi - \varphi_{M^i}) + \mu_0 M_0^i + \frac{K_{C\|}^i}{2M_0^i}\left[3 + \cos 4(\varphi - \varphi_C)\right] + \frac{2K_{U\|}^i}{M_0^i}\sin^2(\varphi - \varphi_U), \tag{3}$$

where $\mu_0 H$ is the Zeeman field, M_0 is the saturation magnetization, $K_{C\|}$ is the in-plane cubic anisotropy constant, $K_{U\|}$ is the in-plane uniaxial anisotropy constant. The interlayer exchange coupling field for layer i is equal to

Table 1. Magnetic materials parameters for the NiFe/CoFe bilayer obtained by simultaneous modelling of the resonance modes (figure 3) and magnetic anisotropies (figure 5) using the Kittel formula (equations (1)–(3)). Listed are the extracted values for the saturation magnetization, M_0, cubic anisotropy constant, $K_{C\|}$, uniaxial anisotropy, $K_{U\|}$, and interlayer exchange coupling field, $\mu_0 H_{ex}$. The values of M_0 and $K_{C\|}$ are compared to literature values for CoFe and NiFe thin films.

	Optical mode	$Co_{0.5}Fe_{0.5}$ [39]	Acoustic mode	$Ni_{0.81}Fe_{0.19}$ [52, 53]
M_0 (kA m^{-1})	1720	1700	900	800
$K_{C\|}$ (kJ m^{-3})	32.0	46.2	2.0	~0
$K_{U\|}$ (kJ m^{-3})	0	—	0.8	—
$\mu_0 H_{ex}$ (mT)	15	—	19.8	—

$$\mu_0 H_{ex}^i = \frac{A_{ex}}{M_0^i d^i} \tag{4}$$

with an interlayer exchange coupling constant A_{ex} (in units of energy/unit area (J m^{-2})) and a layer thickness d. The in-plane angles $\varphi, \varphi_H, \varphi_{M^j}, \varphi_C$, and φ_U correspond to the direction/s of the layer magnetization, external bias field, magnetization in the adjacent layer j, cubic easy axis, and uniaxial easy axis, respectively, with respect to the $Ni_{0.81}Fe_{0.19}$ [100] || $Co_{0.5}Fe_{0.5}$ [110] axes. For the gyromagnetic ratio $\gamma = g\mu_B/\hbar$, where μ_B is the Bohr magneton, we used for both layers a Landé g-factor of $g = 2.1$ [51].

The parameter values, obtained by modelling simultaneously the Kittel curves (figure 3(b)) and the magnetic anisotropies (figures 5(a), (b)), are listed in table 1 and are compared with literature values where appropriate. The perpendicular uniaxial anisotropy (term not included in equations (2) and (3)) was found to be negligible. The angular dependence of the resonance modes in figure 5 requires, apart from cubic and uniaxial anisotropies, an interlayer coupling of $A_{ex} = 0.775$ mJ m^{-2} (same value for both layers). Using in equation (4), d (NiFe) = 43.5 nm and d(CoFe) = 30 nm, this corresponds to $\mu_0 H_{ex}$(NiFe) = 19.8 mT and $\mu_0 H_{ex}$ (CoFe) = 15 mT. We note that a good fit of the Kittel curve for the acoustic mode could only be obtained by including $\mu_0 H_{ex}$, while assuming independent layers without coupling gave an unrealistically large value of the magnetic anisotropy for the NiFe layer.

Table 1 shows that the saturation magnetization obtained for the optical and acoustic modes agree well with the reported values for $Co_{0.5}Fe_{0.5}$ and $Ni_{0.81}Fe_{0.19}$ single layers, respectively. On the other hand, the value for the cubic anisotropy of the CoFe in the bilayer is almost a third smaller than for a single layer. The anisotropy of the NiFe is significantly enhanced compared to the single layer. This suggest the excitation of collective modes, instead of individual layer modes.

4. Characterization of hybrid modes

4.1. XMCD

Figure 6 shows the static XMCD spectra for the Co and Ni $L_{2,3}$ absorption edges with the applied magnetic field along the x-ray beam. The L_3 and L_2 edges correspond to transitions from the respective $2p_{3/2}$ and $2p_{1/2}$ core levels into the unoccupied 3d states, which are spin polarized [33]. At the L_3 edges the XMCD spectra suffer from saturation effects, because the soft x-rays are strongly attenuated on passing through the film which is thicker than the x-ray attenuation length [42]. To alleviate the saturation effects, the XFMR was probed at the photon energy of the less intense L_2 edges (indicated by the arrows in figure 6).

4.2. XFMR

4.2.1. Field scans

In performing XFMR field scans, the RF was set to 8 GHz. The photon energy was tuned to the x-ray absorption edge of the specific element, which was measured by monitoring the luminescence emerging from the MgO substrate. The field sweeps obtained using the XMCD at the Ni, Co, and Fe L_2 edges are shown in figure 7. For each element, the XFMR signal at the resonance peak was maximized by tuning the RF delay time. The signals were normalized per atom using the magnitude of the measured static L_2 XMCD signal. This means that at the resonance we can directly compare the relative contributions of each chemical element.

The field scans show two distinct resonances, namely around 40 mT and 12 mT, as well as an anticipated resonance below 0 mT. The acoustic mode at 40 mT (red arrow) shows that the strongest signal arises from the Ni in the $Ni_{0.81}Fe_{0.19}$ layer, but the Co contributes as well, which confirms that this is a mixed mode. Near 0 mT the Co signal is increased, revealing the leading trail of the optical mode (blue arrow). The field scan for Fe shows that this element is present for both acoustic and optical modes. The middle mode at ~12 mT (green arrow in figure 7) appears only clearly in the Fe signal, which means that it does not originate from the CoFe or NiFe layer.

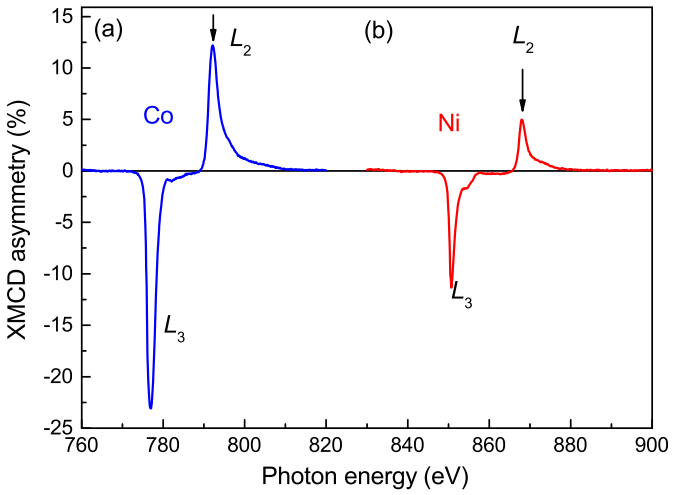

Figure 6. Static XMCD spectra for (a) Co and (b) Ni L_3 and L_2 absorption edges measured in x-ray transmission. The XFMR was monitored at the L_2 edges marked by the arrows.

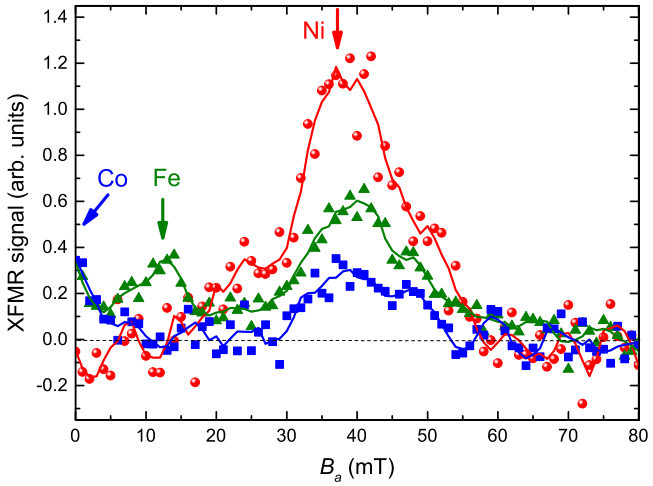

Figure 7. Field scans measured by XFMR at the Ni, Co, and Fe absorption edges of the bilayer with the RF at 8 GHz. The signal was recorded at fixed RF phase corresponding to the maximized XFMR signal at resonance. For each element the XFMR signal was normalized to the static XMCD magnitude. The drawn lines represent a seven-point Savitzky–Golay smooth through the experimental data points (symbols). The three element-specific resonant modes are marked by colour-coded arrows with their main component, although for the Co mode only the leading tail is visible.

Most likely, it has its origin in the 3 nm thick Fe seed layer, which is separated from the NiFe/CoFe bilayer by a 30 nm thick Pt buffer layer. This mode is only visible after the sample has been patterned (cf figure 4), which increases the RF field present in the Fe seed layer. Since both layers in the bilayer film contain Fe, we will present in the following only time-delay scans of the Ni and Co signals, representative of each layer.

4.2.2. Time-delay scans

The precession of the Co and Ni magnetization can be visualized in a direct way by the XFMR time-delay scans. Such scans are obtained at constant driving frequency and bias field using a variable delay time to retard the RF field with respect to the periodic x-ray pulses. As an example, figure 8 shows the delay scans for the acoustic mode (at 37 mT) and the optical mode (at 3 mT) measured at 8 GHz, with the XFMR signal normalized to the static XMCD magnitude for each element. These scans reveal the phase difference between the Ni and Co signals originating from the two separate layers, at the given applied field. Figure 8 shows that at 37 mT the Co phase lags ~7° behind the Ni phase, while at 3 mT this phase lag has increased to ~167°. Thus, the Ni and Co signals are roughly in phase for the acoustic mode and in anti-phase for the optical mode.

In the acoustic mode the Ni signal much is stronger than the Co signal, while the opposite applies to the optical mode (even though its peak maximum is beyond reach at 8 GHz). We can conclude therefore that the

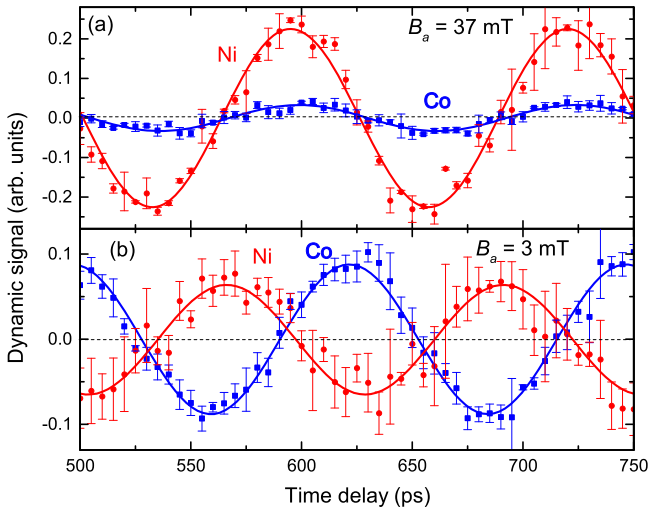

Figure 8. Typical time-delay scans obtained at 8 GHz showing the precession of the Co and Ni spins at (a) 37 mT (acoustic mode) and (b) 3 mT (approaching the optical mode). Shown are single scans without averaging. The XFMR signal has been normalized to the static XMCD magnitude for each element. The solid lines are sinusoidal fits to the data. As seen, at 37 mT (3 mT) the Co phase lags ~7° (~167°) behind the Ni phase. For conversion at 8 GHz, 1 ps corresponds to 3°.

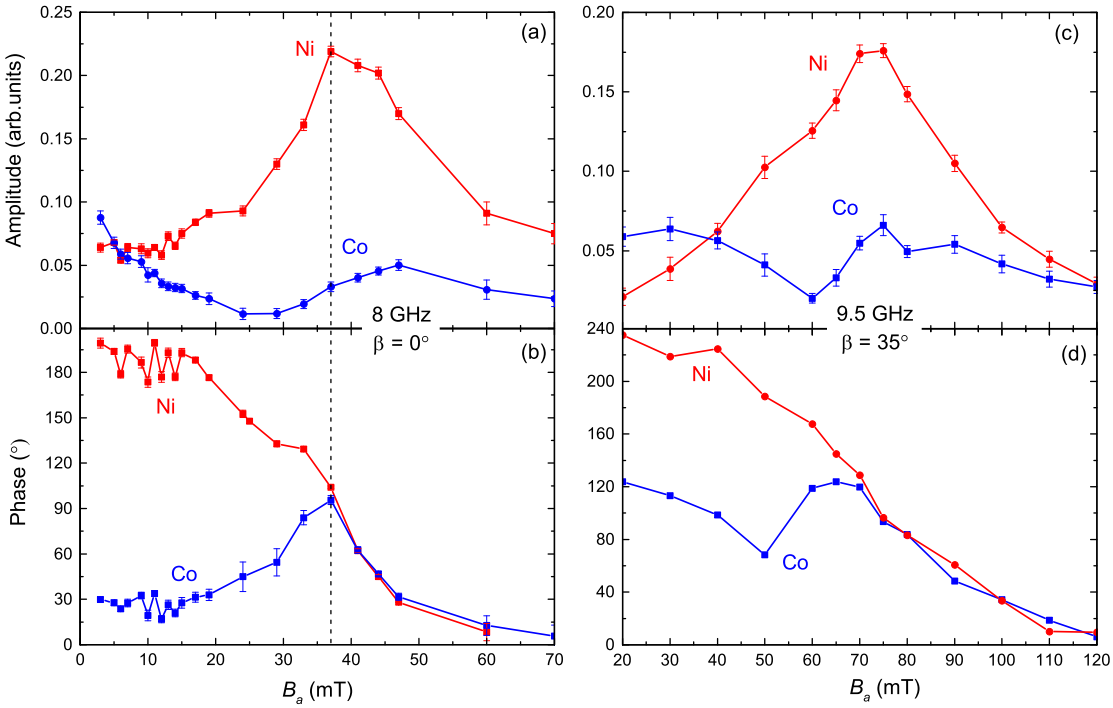

Figure 9. XFMR precessional scans at the Ni and Co L_2 edges as a function of the applied field taken along the CoFe easy axis direction at 8 GHz (left panel) and taken at 35° to the easy axis at 9.5 GHz (right panel). (a), (c) show the amplitudes of the Ni and Co magnetization precession and (b), (d) show their phases with respect to the RF field. The XFMR signal has been normalized per atom to the static XMCD magnitude for each element. The dashed vertical line at 37 mT in (a), (b) indicates the approximate position of the acoustic mode.

acoustic mode is primarily driven by the NiFe layer (figure 8(a)), while the optical mode is primarily driven by the CoFe layer (figure 8(b)). This is in agreement with the results derived from the FMR fitting for the two modes (table 1), however XFMR provides this information in a much more direct way without modelling.

By collecting delay scans of the form shown in figure 8 as a function of the applied field a full picture of the resonant behaviour of the bilayer emerges. The XFMR precessional scans measured at 8 GHz in figure 9(a) display the amplitude and phase of the Ni and Co signals as a function of the applied field. The observed resonance behaviour resembles that of coupled driven harmonic oscillators. Below resonance (i.e., at the high field side) the Ni and Co signals are in phase with the RF field, and this can serve as a reference for the phase of the

driving RF signal. Around 37 mT the resonance of the acoustic mode is reached (dotted vertical line), where the Ni signal is strong in magnitude and ~90° out-of-phase with the driving RF signal. The Co follows the Ni precession in phase up to the Ni signal maximum, at which point the Co phase is lagging 90° behind the RF, so that its amplitude vanishes. Above the Ni resonance (i.e., at the low field side) the Ni signal is in anti-phase with the RF field, i.e., its phase is rotated by ~180°. The Co precession is no longer in phase with that of the Ni, but is in phase with the RF field. Interestingly, the Co, which is dragged by the Ni at resonance, shows a dispersive line shape with its inflection point at the maximum of the Ni amplitude (dashed vertical reference line in figures 9(a) and (b)). As we will discuss in section 5 this is a clear indication of static interlayer exchange coupling. Such a behaviour differs from the resonance response observed for spin pumping in spin valve structures, in which the fixed layer is excited by the resonance of the free layer through a non-magnetic interlayer [30]. Finally, near ~0 T, the Co amplitude increases in the vicinity of the optical resonance.

4.2.3. XFMR along a hard direction

The optical mode can be reached by increasing the RF frequency as well as by tuning the resonance positions using the angular dependence of the magnetic anisotropy. We performed XFMR delay scans at 9.5 GHz with the magnetic field set at $\beta = 35°$, for which the corresponding VNA–FMR field sweep is shown in figure 4(c). Some complications might occur away from the crystal axes, where the magnetization is no longer aligned along the applied field [54]. The more obvious choice of $\beta = 45°$ (i.e., along the hard axis) was not achievable, due to conflicting requirements for XFMR, namely to keep B_{RF} and B_a non-parallel while at the same time maximizing the oscillating magnetization component along the x-ray beam.

At $\beta = 35°$ the resonant fields of the two modes have shifted to larger applied field values (70 mT and 30 mT, respectively). The modes have also moved closer together due to the angular dependence of the magnetic anisotropy (cf figure 5). As a result the modes are more strongly hybridized, so that the acoustic mode contains relatively more CoFe signal than as measured along the easy axis. The acoustic mode in the precessional scan at $\beta = 35°$ (figures 9(c), (d)) shows a comparable behaviour as for $\beta = 0°$ (easy axis), namely the Ni signal changes 180° in phase across the resonance, while the Co signal shows a dispersive shape for the amplitude and a symmetric peak shape for the phase.

What is new in figures 9(c), (d) is the appearance of the optical mode at 30 mT, which is driven by the Co, as confirmed by its increase in amplitude. There is no clear increase in the Ni amplitude since it has a dispersive line shape. Going across the resonance, the Co phase increases by roughly 90° and the Ni phase shows an additional increase from 180°. Hence, both the acoustic and optical mode show a behaviour similar as for coupled harmonic oscillators. Far above resonance (which cannot be reached at 9.5 GHz) both signals will be in anti-phase with the RF, hence the Co phase will further increase to 180°, while the Ni phase will return to 180°.

5. Discussion

For strong enough magnetic coupling between two ferromagnetic layers, the resonance response of the system is represented by collective acoustic and optical modes, which are the in-phase and anti-phase mutual precession modes, respectively. The precession in one layer drags the magnetization of the other layer, and vice versa. The line widths of the resonance peaks depend on the field separation between the modes, which is angular dependent due to the magnetic anisotropy.

The element specificity of XFMR adds substantial benefits to the study of multilayer materials. For instance, when the two layers in a bilayer system are magnetically similar, the averaged FMR signal of the optical mode will be small, since the signals of both layers are in anti-phase and would cancel each other. Roughly speaking, the intensity of the optical mode is proportional to the difference in effective magnetization of the two layers and inversely proportional to the interlayer exchange [55]. However, using the element specificity of XFMR the individual magnetic responses of the two layers become distinguishable. A further unique property of time-resolved XFMR is the visualization of the precession of each individual layer, which allows us to determine the phase lag of each layer with respect to the RF field.

5.1. Static versus dynamic exchange coupling

For the acoustic mode (dashed line in figures 9(a), (b)) the Ni amplitude shows a symmetric peak, whereas the Co amplitude shows a dispersive line shape, i.e., its amplitude has a maximum (minimum) at the high (low) field inflexion point of the Ni amplitude peak. Furthermore, the Co phase shows a symmetric peak at the Ni signal resonance, where the Ni phase passes through 90°. These type of line shapes are the hallmark of static exchange coupling, as will be shown below.

The observed behaviour of the phase and amplitude is different than that for dynamic exchange coupling, as reported by Marcham *et al* [30], where instead the Co amplitude peak is symmetric and the Co phase has a

dispersive shape. Hence the lagged responses of the static and dynamic exchange coupling are completely different. The dynamic coupling is due to spin pumping, which according to the Onsager relations is the reciprocal effect of spin momentum transfer, or STT [37].

In the case of the static exchange coupling the interface energy has the form $U = -A_{ex}\,\mathbf{m}^{(1)} \cdot \mathbf{m}^{(2)}$, where $\mathbf{m}^{(1)}$ and $\mathbf{m}^{(2)}$ are the magnetizations of the two layers and A_{ex} is the interlayer exchange coupling constant. This means that the effective field in the second layer is aligned along the magnetization of the first layer, i.e., $H^{(2)}_{\mathrm{eff,static}} \propto \mathbf{m}^{(1)}$, which is responsible for the observed behaviour of the precessional scans.

Two ferromagnetic layers with a normal metal in between can be exchange coupled by the Ruderman–Kittel–Kasuya–Yosida interaction, which can give rise to giant magnetoresistance. Arena *et al* [35] observed static exchange coupling for a trilayer sample $Ni_{0.81}Fe_{0.19}$(25 nm)/Cu(20 nm)/$Co_{0.93}Zr_{0.07}$(25 nm), in which a weak interlayer coupling arises due to Néel's 'orange peel' magnetostatic interaction [56]. XFMR measurements at the Ni resonance showed a phase increase of ∼35° in the Co response, and modelling the precessional scans resulted in an exchange coupling $A_{ex} = 0.01$ mJ m^{-2} [35]. This should be compared to our NiFe/CoFe bilayer, without Cu interlayer, for which the modelling of the Kittel curves and angular-dependent FMR gives A_{ex}= 0.775 mJ m^{-2}. In our case, A_{ex} has well reached a value where the response in the Co phase of ∼90° is at its 'saturation point'. In the weak coupling case, however, the measured phase increase can provide a sensitive indicator to determine the interlayer exchange coupling constant.

6. Conclusions

Detailed understanding of the magnetization dynamics of an exchange-coupled, epitaxially grown NiFe/CoFe bilayer film has been obtained from a study using SQUID magnetometry, VNA–FMR, combined with XFMR. In particular, time-resolved XFMR allows the two layers to be probed individually, yielding details of the nature, amplitudes, and phases of the two resonant modes. The acoustic mode is characterized by the magnetization of both layers precessing in phase. The amplitude is strongest in the NiFe film, and decays as it penetrates into the CoFe layer. In contrast, the optical mode is characterized by the two layer magnetizations precessing in anti-phase. In this mode the amplitude is strongest in the CoFe layer and spin waves are set up in the NiFe layer.

A detailed analysis of the FMR data shows that the results cannot be simply understood by assuming that the NiFe and CoFe layers are resonating independently. Simultaneous modelling of the measured Kittel curves and the angular dependence emphasizes the need to include an interlayer exchange coupling, as well as a reduced influence of the cubic anisotropy, which agree better with collective mode behaviour. At the Ni signal resonance, the Co signal shows a response in both amplitude and phase. Such features, which are clearly observed in the XFMR precessional scans, can be ascribed to the presence of an interface exchange coupling between both layers.

The damping mechanisms in magnetization dynamics typically incorporate energy transfer between different reservoirs in a magnetic system, which manifests itself by a phase lag between the different constituents [57]. The element-specific precessional scans of the NiFe/CoFe bilayer clearly show the signature of static exchange coupling, in which the effective field in one layer is aligned along the magnetization direction of the other layer.

We have also demonstrated the uniqueness of the XFMR method by showing that the observed middle mode can be ascribed to a resonance of the Fe seed layer, instead of originating from the Fe in the bilayer, since it is not accompanied by a resonance of the Co or Ni signal. Such a result cannot be obtained from any other technique. It means that in relatively complex layer stacks the resonance can be decomposed into elemental contributions. By normalizing the XFMR signal to the static XMCD, the signal amplitude per atom can be obtained.

We expect that our results will give a further stimulus to the initiation of theoretical modelling of the Gilbert damping and spin pumping in layered magnetic structures. Gaining a deeper understanding of the magnetic behaviour of such systems will expedite their use in technological applications.

Acknowledgments

Diamond Light Source is acknowledged for allocating beamtime on the I06 branch line and Helmholtz-Zentrum Berlin for beamtime on PM3 at BESSY II. The research leading to these results has received funding from the European Community's Seventh Framework Programme (FP7) under grant agreement no. 312284 and the German Federal Ministry of Education and Research (BMBF) through grant no. 05K13WR1 (VEKMAG project). We thank G Ashton, H Fangohr C J Kinane, L C Maple, and R C C Ward for help and discussions during the course of this work.

References

[1] Suess D, Schrefl T, Fahler S, Kirschner M, Hrkac G, Dorfbauer F and Fidler J 2005 Exchange spring media for perpendicular recording *Appl. Phys. Lett.* **87** 012504

[2] Suess D, Schrefl T, Dittrich R, Kirschner M, Dorfbauer F, Hrkac G and Fidler J 2005 Exchange spring recording media for areal densities up to 10 Tbit/in^2 *J. Magn. Magn. Mater.* **290** 551–4

[3] Victora R H and Shen X 2005 Composite media for perpendicular magnetic recording *IEEE Trans. Magn.* **41** 537–42

[4] Skomski R and Coey J M D 1993 Giant energy product in nanostructured 2-phase magnets *Phys. Rev.* B **48** 15812–6

[5] Skomski R and Coey J M D 1993 Nucleation field and energy product of aligned 2-phase magnets—progress towards the '1 MJ/m^3' magnet *IEEE Trans. Magn.* **29** 2860–2

[6] Gibbs M R J 2005 Applications of magmems *J. Magn. Magn. Mater.* **290** 1298–303

[7] Ludwig A and Quandt E 2000 Giant magnetostrictive thin films for applications in microelectromechanical systems *J. Appl. Phys.* **87** 4691–5

[8] Pan C T and Shen S C 2005 Magnetically actuated bi-directional microactuators with permalloy and Fe/Pt hard magnet *J. Magn. Magn. Mater.* **285** 422–32

[9] Suess D, Lee J, Fidler J and Schrefl T 2009 Exchange-coupled perpendicular media *J. Magn. Magn. Mater.* **321** 545–54

[10] Shaw J M, Nembach H T and Silva T J 2011 Damping phenomena in $Co_{90}Fe_{10}$/Ni multilayers and alloys *Appl. Phys. Lett.* **99** 012503

[11] Cochran J F, Heinrich B and Arrott A S 1986 Ferromagnetic-resonance in a system composed of a ferromagnetic substrate and an exchange-coupled thin ferromagnetic overlayer *Phys. Rev.* B **34** 7788–801

[12] Metaxas P J, Stamps R L, Jamet J-P, Ferre J, Baltz V, Rodmacq B and Politi P 2010 Dynamic binding of driven interfaces in coupled ultrathin ferromagnetic layers *Phys. Rev. Lett.* **104** 237206

[13] Magaraggia R, Kennewell K, Kostylev M, Stamps R L, Ali M, Greig D, Hickey B J and Marrows C H 2011 Exchange anisotropy pinning of a standing spin-wave mode *Phys. Rev.* B **83** 054405

[14] Kaiser A M *et al* 2011 Nano and picosecond magnetization dynamics of weakly coupled CoFe/Cr/NiFe trilayers studied by a multitechnique approach *Phys. Rev.* B **84** 134406

[15] Timopheev A A, Pogorelov Yu G, Cardoso S, Freitas P P, Kakazei G N and Sobelev N A 2014 Dynamic exchange via spin currents in acoustic and optical modes of ferromagnetic resonance in spin-valve structures *Phys. Rev.* B **89** 144410

[16] Heinrich B, Purcell S T, Dutcher J R, Urquhart K B, Cochran J F and Arrott A S 1988 Structural and magnetic properties of ultrathin Ni/Fe bilayers grown epitaxially on Ag(001) *Phys. Rev.* B **38** 12879–96

[17] Zhang Z, Zhou I, Wigen P E and Ounadjela K 1994 Angular-dependence of ferromagnetic-resonance in exchange-coupled Co/Ru/Co trilayer structures *Phys. Rev.* B **50** 6094–112

[18] Gómez J, Weston J L and Butera A 2007 Ferromagnetic coupled modes in continuous/granular multilayers: model and experiments *Phys. Rev.* B **76** 184416

[19] Martin T, Woltersdorf G, Stamm C, Dürr H A, Mattheis R, Back C H and Bayreuther G 2008 Layer resolved magnetization dynamics in interlayer exchange coupled $Ni_{81}Fe_{19}$/Ru/$Co_{90}Fe_{10}$ by time resolved x-ray magnetic circular dichroism *J. Appl. Phys.* **103** 07B112

[20] Goulon J, Rogalev A, Wilhelm F, Jaouen N, Goulon-Ginet C, Goujon G, Youssef J B and Indendom M V 2005 X-ray detected magnetic resonance at the Fe *K*-edge in YIG: forced precession of magnetically polarized orbital components *JETP Lett.* **82** 696–701

[21] Goulon J, Rogalev A, Wilhelm F, Jaouen N, Goulon-Ginet C and Brouder C 2006 X-ray detected ferromagnetic resonance in thin films *Eur. Phys. J.* B **53** 169–84

[22] Guan Y, Bailey W E, Kao C-C, Vescovo E and Arena D A 2006 Comparison of time-resolved x-ray magnetic circular dichroism measurements in reflection and transmission for layer-specific precessional dynamics measurements *J. Appl. Phys.* **99** 08J305

[23] Guan Y, Bailey W E, Vescovo E, Kao C-C and Arena D A 2007 Phase and amplitude of element-specific moment precession in $Ni_{81}Fe_{19}$ *J. Magn. Magn. Mater.* **312** 374–8

[24] Boero G, Mouaziz S, Rusponi S, Bencok P, Nolting F, Stepanow S and Gambardella P 2008 Element-resolved x-ray ferrimagnetic and ferromagnetic resonance spectroscopy *New J. Phys.* **10** 013011

[25] Boero G, Rusponi S, Bencok P, Meckenstock R, Thiele J-M, Nolting F and Gambardella P 2009 Double-resonant x-ray and microwave absorption: atomic spectroscopy of precessional orbital and spin dynamics *Phys. Rev.* B **79** 224425

[26] Boero G, Rusponi S, Kavich J, Rizzini A L, Piamonteze C, Nolting F, Tieg C, Thiele J-U and Gambardella P 2009 Longitudinal detection of ferromagnetic resonance using x-ray transmission measurements *Rev. Sci. Instrum.* **80** 123902

[27] Goulon J, Rogalev A, Wilhelm F, Goujon G, Brouder C, Yaresko A, Youssef J B and Indenbom M V 2010 X-ray detected magnetic resonance of YIG thin films in the nonlinear regime of spin waves *J. Magn. Magn. Mater.* **322** 2308–29

[28] Arena D A, Ding Y, Vescovo E, Zohar S, Guan Y and Bailey W E 2009 A compact apparatus for studies of element and phase-resolved ferromagnetic resonance *Rev. Sci. Instrum.* **80** 083903

[29] Marcham M K *et al* 2011 Phase-resolved x-ray ferromagnetic resonance measurements in fluorescence yield *J. Appl. Phys.* **109** 07D353

[30] Marcham M K *et al* 2013 Phase-resolved x-ray ferromagnetic resonance measurements of spin pumping in spin valve structures *Phys. Rev.* B **87** 180403(R)

[31] Bailey W E, Cheng C, Knut R, Karis O, Auffret S, Zohar S, Keavney D, Warnicke P, Lee J-S and Arena D A 2013 Detection of microwave phase variation in nanometre-scale magnetic heterostructures *Nat. Commun.* **4** 2025

[32] Marcham M K *et al* 2013 Influence of a Dy overlayer on the precessional dynamics of a ferromagnetic thin film *Appl. Phys. Lett.* **102** 062418

[33] van der Laan G and Thole B T 1991 Strong magnetic x-ray dichroism in 2*p* absorption–spectra of 3*d* transition-metal ions *Phys. Rev.* B **43** 13401–11

[34] van der Laan G 2013 Applications of soft x-ray magnetic dichroism *J. Phys.: Conf. Ser.* **430** 012127

[35] Arena D A, Vescovo E, Kao C C, Guan Y and Bailey W E 2006 Weakly coupled motion of individual layers in ferromagnetic resonance *Phys. Rev.* B **74** 064409

[36] Arena D A, Vescovo E, Kao C-C, Guan Y and Bailey W E 2007 Combined time-resolved x-ray magnetic circular dichroism and ferromagnetic resonance studies of magnetic alloys and multilayers (invited) *J. Appl. Phys.* **101** 09C109

[37] Tserkovnyak Y, Brataas A, Bauer G E W and Halperin B I 2005 Nonlocal magnetization dynamics in ferromagnetic heterostructures *Rev. Mod. Phys.* **77** 1375–421

[38] Warnicke P, Knut R, Wahlström E, Karis O, Bailey W E and Arena D A 2013 Exploring the accessible frequency range of phase-resolved ferromagnetic resonance detected with x-rays *J. Appl. Phys.* **113** 033904

[39] Kuschel T, Hamrle J, Pištora J, Saito K, Bosu S, Sakuraba Y, Takanashi K and Wollschläger J 2012 Magnetic characterization of thin $Co_{50}Fe_{50}$ films by magnetooptic Kerr effect *J. Phys. D: Appl. Phys.* **45** 495002

[40] Dunsmore J P 2012 *Handbook of Microwave Component Measurements: With Advanced VNA Techniques* (Chichester: Wiley)
[41] Beaujour J M L, Kent A D, Abraham D W and Sun J Z 2008 Ferromagnetic resonance study of polycrystalline $Fe_{1-x}V_x$ alloy thin films *J. Appl. Phys.* **103** 07B519
[42] van der Laan G and Figueroa A I 2014 X-ray magnetic circular dichroism—a versatile tool to study magnetism *Coord. Chem. Rev.* **277–278** 95–129
[43] Landau L D, Lifshitz E M and Pitaevski L P 1980 *Statistical Physics, Part 2* (Oxford: Pergamon)
[44] Kittel C 1948 On the theory of ferromagnetic resonance absorption *Phys. Rev.* **73** 155–61
[45] Mosendz O, Pearson J E, Fradin F Y, Bader G E W and Hoffmann A 2010 Quanrifying spin Hall angles from spin pumping: experiment and theory *Phys. Rev. Lett.* **104** 046601
[46] Arenholz E and Prestemon S O 2005 Design and performance of an eight-pole resistive magnet for soft x-ray magnetic dichroism measurements *Rev. Sci. Instrum.* **76** 083908
[47] Thomas C A, Rehm G, Owen H L, Wyles N G, Botchway S W, Schlott V and Wahl M 2006 Bunch purity measurements for diamond *Nucl. Instrum. Methods Phys. Res.* A **566** 762–6
[48] Vaz C A F, Moutafis C, Buzzi M and Raabe J 2013 X-ray excited optical luminescence of metal oxide single crystals *J. Electron Spectrosc. Relat. Phenom.* **189** 1–4
[49] Sakshath S, Bhat S V, Kumar P S A, Sander D and Kirschner J 2011 Enhancement of uniaxial magnetic anisotropy in Fe thin films grown on GaAs(001) with MgO underlayer *J. Appl. Phys.* **109** 07C114
[50] Woltersdorf G 2004 Spin-pumping and two-magnon scattering in magnetic multilayers *PhD Thesis* Simon Fraser University, Vancouver, Canada
[51] Reck R A and Fry D L 1969 Orbital and spin magnetization in Fe-Co, Fe-Ni, and Ni-Co *Phys. Rev.* **184** 492–5
[52] Counil G, Kim J-V, Devolder T, Chappert C, Shigeto K and Otani Y 2004 Spin-wave contributions to the high-frequency magnetic response of thin films obtained with inductive methods *J. Appl. Phys.* **95** 5646–52
[53] Madami M, Tacchi S, Gubbiotti G, Bonanni V, Bisero D, Vavassori P, Adeyeye A O, Goolaup S, Singh N and Spezzani C 2009 Magnetization reversal and spin waves in exchange coupled NiFe/Cu/Co nanodisks *J. Appl. Phys.* **105** 07C115
[54] Dürr H A and van der Laan G 1996 Magnetic circular x-ray dichroism in transverse geometry: importance of noncollinear ground state moments *Phys. Rev.* B **54** 760–3
[55] Lindner J and Baberschke K 2003 In situ ferromagnetic resonance: an ultimate tool to investigate the coupling in ultrathin magnetic films *J. Phys.: Condens. Matter.* **15** R193–232
[56] Néel L 1962 Magnetism—sur un nouveau mode de couplage entre les animantations de deux couches minces ferromagnetiques *C. R. Acad. Sci.* **255** 1676
[57] Sparks M 1965 *Ferromagnetic Relaxation Theory* (New York: McGraw-Hill)